Mathematical Biosciences 366 (2023) 109088

Contents lists available at ScienceDirect

Mathematical Biosciences

journal homepage: www.elsevier.com/locate/mbs

Original Research Article

Mathematical birth of Early Afterdepolarizations in a cardiomyocyte model

R. Barrio [a,*], J.A. Jover-Galtier [a], M.A. Martínez [a], L. Pérez [b], S. Serrano [a]

[a] IUMA, CoDy and Dpto. Matemática Aplicada, Universidad de Zaragoza, E-50009 Zaragoza, Spain
[b] Dpto. Matemáticas, University of Oviedo, Oviedo E-33007, Spain

ARTICLE INFO

MSC:
92B05
34C23
34Cxx

Keywords:
Cardiac dynamics
Early Afterdepolarizations (EADs)
Bifurcations
Isolas
Fast–slow decomposition

ABSTRACT

Early Afterdepolarizations (EADs) are abnormal behaviors that can lead to cardiac failure and even cardiac death. In this paper we investigate the occurrence and development of these phenomena in a reduced Luo–Rudy cardiac model. Through a comprehensive dynamical analysis, we map out the distinct patterns observed in the parametric plane, differentiating between normal beats without EADs and pathological beats with EADs. By examining the bifurcation structure of the model, we elucidate the dynamical elements associated with these patterns and their transitions. Using a fast–slow analysis, we explore the emergence and evolution of EADs in the model. Notably, our approach combines the two commonly used fast–slow approaches (1-slow–2-fast and 2-slow–1-fast), and we show how both approaches together provide a more complete understanding of this phenomenon.

1. Introduction

Heart cells are excitable cells. This means that they carry out their functions by generating electrical signals that are determined by the change in the potential of the cell membrane. Each of these electrical signals is called an action potential (AP), so in order to study the behavior of a cardiac cell we have to study the dynamics of its APs. The AP has several phases, in phase-0 the potential increases rapidly until it reaches a maximum of depolarization, in phase-1 the potential decreases slightly (transient repolarization), in phase-2 the potential remains constant (plateau) and finally in phase-3 it goes down (repolarization) until it reaches the resting potential that would be phase-4. Under certain conditions, in phase-2 and/or phase-3, there is a small rise in potential, which is known as phase-2 or phase-3 early afterdepolarization (EAD). Phase-2 EADs occur during phase-2 of the AP, at values of the potential typically above −40 mV [1], on the plateau of the bursting orbit (see Fig. 1). If EADs at cellular level are of large enough magnitude and occur over a substantial tissue area, they can lead to triggered activity and arrhythmias, which makes their study highly relevant.

APs can be described mathematically as a set of ordinary differential equations that model the various currents entering and leaving the cell. In 1991 Luo and Rudy [2] proposed a model of a mammalian ventricle. Since this model reproduces many behaviors and we are only interested in studying the appearance and evolution of EADs, the model can be simplified by following [3,4]. In [5] we have compared the results obtained in a high dimensional model with a simplified model and we have seen that the simple one perfectly explains what we find in the more biophysically complete model. Therefore, the analysis of reduced models of the original one is valid for studying the behavior of EADs, as other authors have already done in previous works [6–10]. Moreover, we keep only the calcium and potassium current since the sodium current included in the original model corresponds to a fast current that does not influence neither phase 2 or 3, which is where these EADs can appear. Finally, we work with a three-variable model. It is a very simplified model, but it is capable of simulating the appearance of EADs.

In particular, the reduced version of the Luo and Rudy (LR) model we consider can be described by a 3D ODE system:

$$\begin{cases} C_m \dfrac{dV}{dt} = -(I_{Ca} + I_K), \\ \dfrac{df}{dt} = \dfrac{f_\infty(V) - f}{\tau_f}, \\ \dfrac{dx}{dt} = \dfrac{x_\infty(V) - x}{\tau_x}, \end{cases} \tag{1}$$

where C_m is the membrane capacitance which was set at $0.5\,\mu F/cm^2$; V is the potential of the cell membrane; f is the inactivation gating variable for the calcium current; and x the activation gating variable for the potassium current. We consider the two main ionic currents (I_{Ca},

* Corresponding author.
E-mail addresses: rbarrio@unizar.es (R. Barrio), jorgejover@unizar.es (J.A. Jover-Galtier), gelimc@unizar.es (M.A. Martínez), perezplucia@uniovi.es (L. Pérez), sserrano@unizar.es (S. Serrano).

https://doi.org/10.1016/j.mbs.2023.109088
Received 13 April 2023; Received in revised form 20 September 2023; Accepted 17 October 2023
Available online 19 October 2023

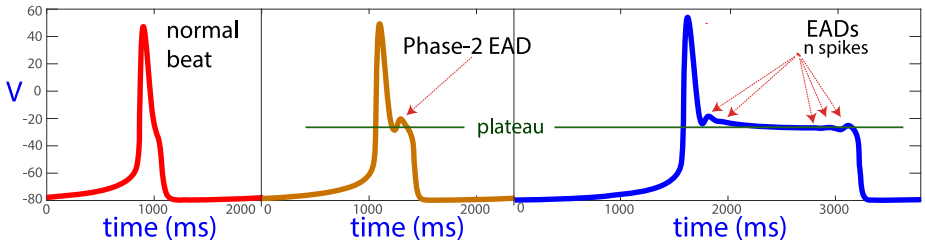

Fig. 1. Normal AP, phase-2 EAD with one extra spike and phase-2 EADs with n extra spikes on the phase-2 plateau of the AP.

Table 1
The fixed parameter values [11] used along the paper, unless stated otherwise.

$C_m = 0.5\ \mu F/cm^2$			
$G_K = 0.04$ mS/cm^2	$\tau_x = 300$ ms	$\theta_x = 5$ mV	$E_x = -40$ mV $E_K = -80$ mV
$G_{Ca} = 0.025$ mS/cm^2	$\tau_f = 80$ ms	$\theta_f = 8.6$ mV $\theta_d = 6.24$ mV	$E_f = -20$ mV $E_d = -35$ mV $E_{Ca} = 100$ mV

a slow inward current; and I_K, a time-dependent potassium current); both computed for 1 cm^2 of membrane. The two ionic currents and the steady state functions are defined by

$$I_{Ca} = G_{Ca} \cdot d_\infty(V) \cdot f \cdot (V - E_{Ca}); \qquad I_K = G_K \cdot x \cdot (V - E_K);$$

$$f_\infty(V) = \frac{1}{1 + e^{\frac{V - E_f}{\theta_f}}}, \quad x_\infty(V) = \frac{1}{1 + e^{\frac{E_x - V}{\theta_x}}}, \quad d_\infty(V) = \frac{1}{1 + e^{\frac{E_d - V}{\theta_d}}},$$

where G_{Ca} and G_K are the calcium and potassium channel conductance; E_{Ca} and E_K are the reversal potential of calcium and potassium; d_∞ is the steady state function for the calcium current activation gating variable, d, which has been replaced by its steady state function in the simplification of [11]. The parameter values used in this article are given in Table 1.

In [7] a first preliminary analysis of the bifurcations of the model was developed. A subsequent more detailed analysis [12] detected isolas of periodic orbits that organize the different patterns of EADs. However, a more in-depth analysis of the different bifurcations existing in the model dynamics and how these bifurcations influence the type of generation of new EADs remained pending. In this paper we address these issues in a comprehensive manner.

In terms of dynamics, this system can be described as a "fast–slow dynamical system" with three distinct time scales. The variable V evolves the quickest, while x changes the slowest, and f falls in between as an intermediate variable. There have been two different approaches used to analyze this system. The first approach, as shown in [6,13], treats the intermediate variable as a fast variable. Similar methodologies have been employed in mathematical neuron models, such as those discussed in [14–16], where bifurcations in the two-dimensional fast subsystem are linked to the classification of bursting models and the generation of new oscillations (spikes). Although this approach has been effective in studying the presence or absence of EADs in various cardiac studies, recent findings have revealed its limitations in providing accurate analysis in certain situations [7]. To gain further understanding of how EADs are affected by pacing frequency or pharmacological interventions, an alternative approach was introduced in previous studies [7,8,12]. This approach treats the intermediate variable as a slow variable, leading to a 2-slow–1-fast decomposition. By considering this perspective, we ask ourselves the following question: can the 1-slow–2-fast decomposition complement this second approach? In our work, we combine both approaches in order to describe the observed behavior of the system. After a standard 2-slow–1-fast analysis, we notice how the evolution of the system along the critical manifold S_0 also presents a fast–slow behavior. Thus, we separate the two slow variables in a slow variable and an ultra-slow variable, computing in this situation the corresponding critical manifold $\bar{S}_0$ for the 1-slow–2-fast analysis. Both S_0 and $\bar{S}_0$ are relevant in the description of the observed dynamical properties of the system, which cannot be properly understood with only one of them. Note that in literature the use of three time scales have been deeply studied in [17–21] for mathematical neuron models. We show that in cardiomyocyte models is also relevant.

The paper is organized as follows. In Section 2 we present a study of the bifurcations in the reduced Luo–Rudy model and we show how the EADs appear and evolve in the different identified regions and we explain the bifurcation structure in the EADs adding processes using continuation techniques. Section 3 is devoted to show the role of the different fast–slow decompositions. Lastly, we present our conclusions at the end of the paper.

2. Bifurcation structure of the model

In this section we provide a study of the bifurcations of the LR system (1). In previous works [6,7,12], variations in cell capacitance, C_m, and conductances of the calcium, G_K, and potassium currents, G_{Ca}, were used to analyze their influence on the occurrence of EADs. Here we consider the biparametric plane (G_K, E_f) to introduce a new parameter and see if the situation is similar to that observed in these previous studies. E_f is the inactivation parameter of the calcium current and enters into the calculation of f_∞ and therefore of f. Actually, to modify E_f is another way to modify the I_{Ca} current. Moreover, this parameter can be experimentally varied. There are studies [22,23] where they discuss the existence of pharmacological modulators that can shift the activation or inactivation voltage. For example, some agonists can shift the inactivation voltage downwards, while antagonists shift it upwards. There are also other techniques [24] known as post-translational modulation that can affect this voltage. The rest of the parameters are fixed as outlined in Table 1. This study allows us to identify the dynamical elements responsible to the appearance of EADs.

In Fig. 2 we study this plane using the spike-counting technique and also providing a biparametric continuation (using the well-known software AUTO [25,26]) of Hopf (pink) and homoclinic bifurcation (red and yellow) curves. All of them refer to the equilibrium point (V_e, f_e, x_e) with V_e solution of the equation

$$G_{Ca} \cdot d_\infty(V_e) \cdot f_\infty(V_e) \cdot (V_e - E_{Ca}) + G_K \cdot x_\infty(V_e) \cdot (V_e - E_K) = 0$$

and $f_e = f_\infty(V_e)$ and $x_e = x_\infty(V_e)$. Regarding the spike-counting technique, the color indicates the number of maxima on each period of the periodic orbits and this is the number of spikes per orbit. Therefore, in pictures (a–c), dark blue color (bottom and sides in (a)) denotes a dead cell (convergence to equilibria), blue (1 spike) is the normal beat with just the large spike (almost the entire inner region bounded by the Hopf bifurcation pink curve), and, in the rest of cases (small triangular region in (a)), orbits with EADs. Picture (a) shows an overview of the parametric plane. Outside the Hopf bifurcation curve, the equilibrium (V_e, f_e, x_e) is stable and attracts the dynamics of the system, so there is no beat. At the Hopf bifurcation, the stability of the equilibrium changes and periodic orbits appear in the inner region giving rise

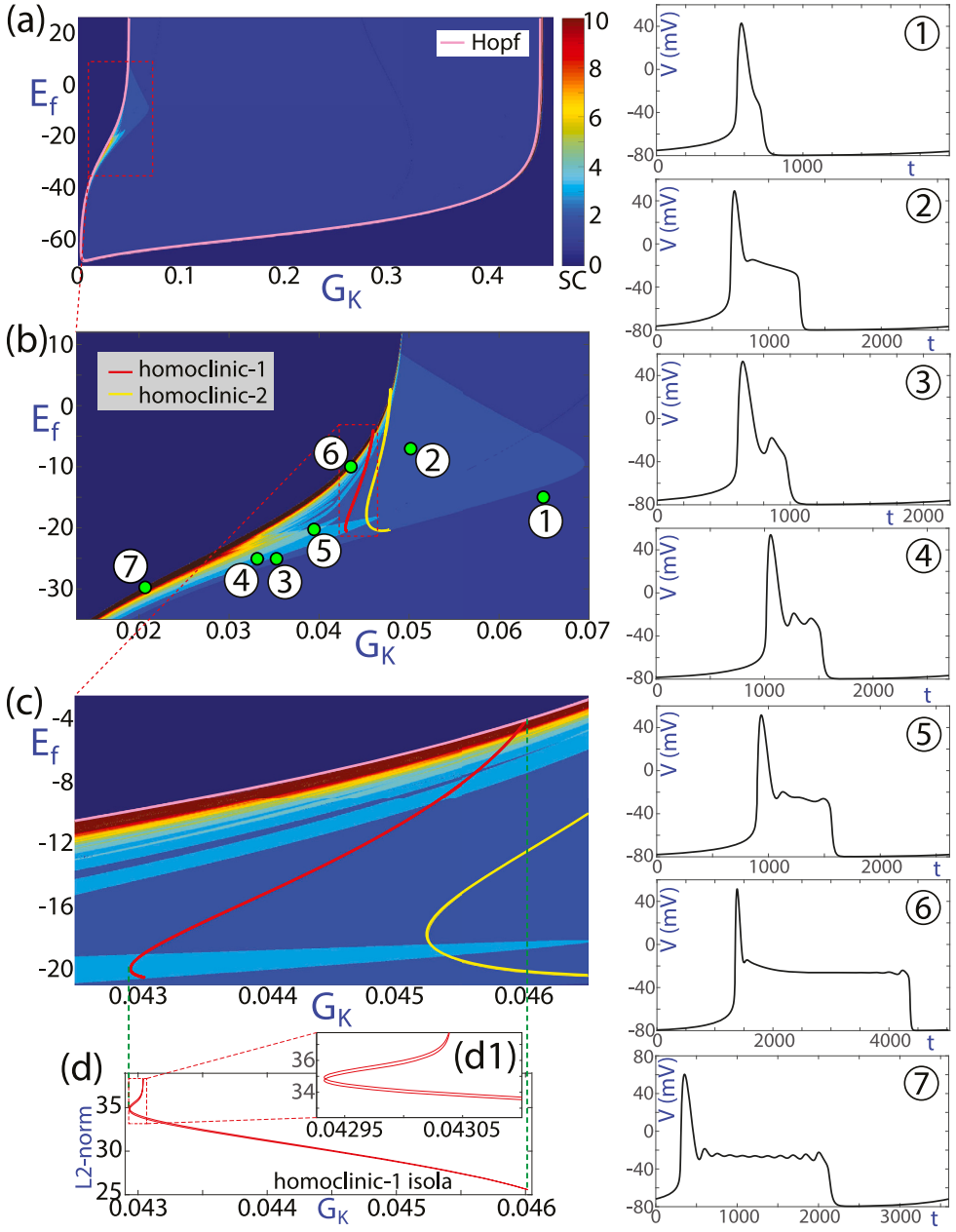

Fig. 2. (a) Spike-counting on the (G_K, E_f) parameter plane showing two different regions: outside Hopf bifurcation pink curve, dynamics converges to a point of equilibrium, dead cell; inside, the dynamics of the cell undergoes APs with or without EADs. (b) Magnification of the triangular shape EAD region where the spike-adding phenomenon occurs. Green points and numbers mark the values for the time series represented in right plots. (c) Magnification of the region where red homoclinic-1 bifurcation is located. (d) The red homoclinic-1 loop is shown in the AUTO L_2 norm. The small plot (d1) is a zoom of the upper part showing that it is a closed loop.

to APs. Plot (b) shows the triangular region with several changes in the number of spikes of the periodic orbits. In addition, small green dots accompanied by a number indicate the parametric position of the values taken for different time series represented in the right column as an example. We see in these examples how the different number of spikes translates into a different number of EADs. Note that throughout the triangular region the situation, in terms of the number of spikes, is analogous for any value of E_f. As we enter the region from the right, we move from an orbit with no EAD to an orbit in which there is an EAD in each AP. Subsequently, as we move further to the left edge of the triangular zone, more EADs appear in each AP of the periodic orbit. The only appreciable difference is the amplitude in G_K of the different windows with different number of EADs as we move away from the value of $E_f = -20$ mV (classical value). The existence of homoclinic curves does not seem to influence the number of spikes in the orbits. However, we will see later that (red) homoclinic-1 plays an important role in the type of generation of new EADs. In picture (c) we show a magnification of the region where red homoclinic-1 curve exists. Moreover, from this picture, one can suspect that each homoclinic curve ends at two points. In fact, this is not true as the curve is really a closed loop with very sharp turns. The small plots (d) and (d1) detail this fact. On (d) we have the AUTO continuation showing the L_2 norm and (d1) is a zoom that illustrates clearly that we really have a closed loop.

As it seems that the behavior within the triangular region is analogous for any value of E_f, we will focus for the moment on the classical line (with $E_f = -20$ mV). We are interested in seeing how the periodic orbits evolve changing G_K. We show, in Fig. 3 on the plot (a), the bifurcation diagram obtained by varying this parameter. The red points on the top part of the bifurcation diagram correspond to the AP peaks

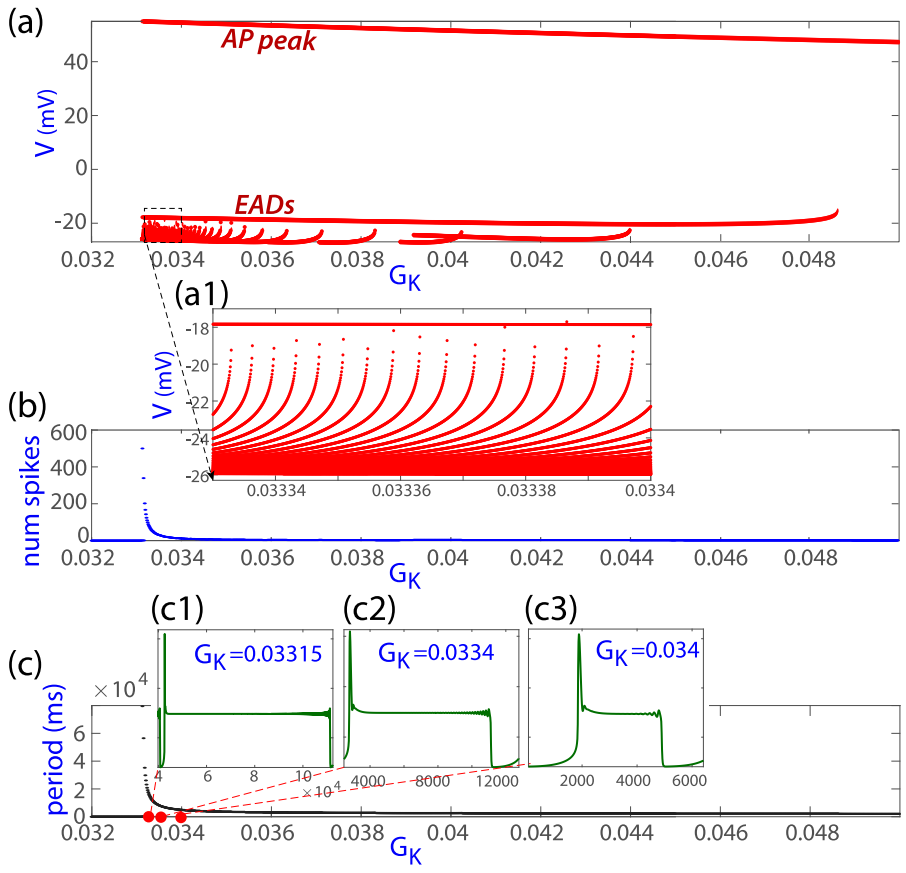

Fig. 3. (a) Bifurcation diagram obtained by varying G_K (with fixed $E_f = -20$ mV). The red points on the top part of the bifurcation diagram correspond to the AP peaks and those on the bottom part correspond to the EAD peaks. The magnification (a1) shows the spike adding process increasing the number of EADs when moving to the left. Plot (b) presents the number of spikes showing their increase. Plot (c) gives the period. The small plots (c1–c3) show the time series at three values of G_K illustrating the increment in the period and in the number of EADs.

and those on the bottom part correspond to the EAD peaks. On the left part of the plot, no red points appear as this area corresponds to the region where the equilibrium point is stable and the cell is dead (no APs). Starting in the right zone, there are no points in the lower zone because, for those values of G_K, the APs do not have EADs. It is at a value of G_K close to 0.049 that the first EAD begins to appear. Further to the left other EADs are appearing. We observe, from the magnification on plot (a1) that, moving from right to the left, more extra curves (and, therefore, more EAD peaks) appear until the left boundary of the triangular region is reached. The limit of the existence of the periodic orbits on the left side is related with a Hopf bifurcation of the depolarized equilibrium point, and then becoming stable and attracting most of the dynamics. The plot (b) shows the number of spikes in each AP. The increase in the number of spikes (and thus of EADs) is evident as G_K decreases. In addition, the rate of growth in the number of EADs is increasing as we approach the value at which the left edge of the triangular region is reached. On plot (c) we show the period of the periodic orbits, which coincides with the duration of the AP. On the small insets (c1,c2,c3) we give time series of three periodic orbits at different values of G_K. On these plots we can observe the increment in the number of small spikes (EADs) and the increment in time, staying a quite long time on the plateau of the phase 2 of the AP. Note that the cardiac fibrilation is related with the situation where the cardiomyocyte always, or a long time, stays on a small oscillation regime.

2.1. EAD transitions: continuous and isola cases

Above, we have got a "roadmap" locating the different regimes (AP loss, normal AP and AP with EADs) in the biparametric plane (Fig. 2). However, how and where exactly do the EADs appear? To answer this question, in Fig. 4 we show a continuation of the equilibria and limit cycles obtained using software AUTO on the reference line $E_f = -20$ mV. The curve of equilibria is depicted in black, the red points are Hopf bifurcation points (the two intersections of the straight line $E_f = -20$ mV with the Hopf bifurcation curve), black points are homoclinic bifurcation points and the rest of the diagram consists of different families of periodic solutions. Continuous line indicates stability and discontinuous line indicates unstability of the invariant objects. In plot (a) the x axis represents the bifurcation parameter G_K and in the y axis the AUTO L_2 norm. We can observe how a stable family of periodic orbits (in blue) is born from the right supercritical Hopf bifurcation point. This is the origin of the normal beat in the model. It is in the left-hand zone that numerous changes in the nature of periodic orbits occur. To better observe what takes place in that region, we show in panel (b) a magnification of the bifurcation diagram. Panels (d) and (e) show different views of the same bifurcation diagram. Specifically, panel (d) shows the period, while panel (e) shows the maximum and minimum potential, V, of the corresponding periodic orbit. Panel (c) is a magnification of (b) for the region where homoclinic bifurcation points take place. We can observe in panels (b) and (c) how the periodic orbit touches the equilibrium point at the homoclinic bifurcation, while in panel (d) the period grows indefinitely as we approach these points. In contrast, in panel (e) the only thing we observe is the sudden disappearance of these families, but without an obvious explanation from this representation. Note that these two homoclinic bifurcation points correspond to the intersection of the reference line $E_f = -20$ mV with each of the two homoclinic bifurcation curves shown in Fig. 2.

With the information provided by the bifurcation diagrams, we have the following scenario. First, we go from right to left in the

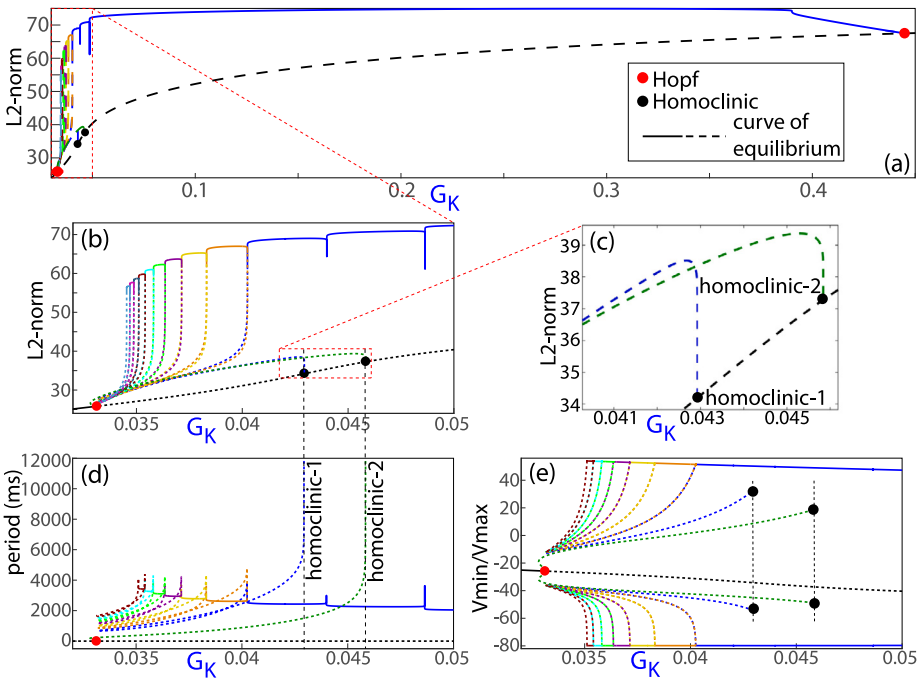

Fig. 4. Bifurcation diagram on the G_K parametric line ($E_f = -20$ mV) obtained using continuation software AUTO. Equilibrium curve is represented in black. (a) Periodic orbits (color curves) are created and destroyed at two Hopf bifurcation (red) points. Continuous lines stands for stable invariants, where discontinuous ones unstable. The region with EADs is located on the left side. (b) Magnification of the region with EADs. Black points represent homoclinic bifurcation points for blue and green families of periodic orbits. (c) Magnification of (b) in the region where blue and green family of periodic orbits touch the equilibrium. (d) Same as (b) showing period of periodic orbit instead of AUTO L_2 norm. (e) Same as (b) and (d) showing maximum and minimum of V.

bifurcation diagram. For large values of G_K, there is a stable family of equilibria (the black curve), which becomes unstable at a supercritical Hopf bifurcation point for $G_K \approx 0.445$. At this point, a family of stable periodic orbits, the blue curve, is born. This family presents two sudden fall downs (see Fig. 4(b)), which are actually very sharp loops, at $G_K \approx 0.0486$ and $G_K \approx 0.044$. If we look at Fig. 3(a), we can see how these loops correspond to the appearance of the first and second EAD, respectively. As G_K becomes smaller, the blue curve loses its stability. The unstable branch evolves towards a value close to the left Hopf bifurcation point, turns to the right and ends up disappearing at the homoclinic-1 bifurcation point. Along the unstable part of the family, the shape of the periodic (unstable) orbits evolves, but the number of orbit peaks remains constant and equal to three. Approximately at the value at which the blue family loses its stability, a new (orange) family of periodic orbits appears. The curve corresponding to this family is an isola, that is, a simple closed curve of periodic orbits. For smaller values of G_K, there is a sequence of (different color) isolas of periodic orbits, all of them with a stable branch (at the top) and a unstable branch. The smaller the value of G_K the smaller the isolas and the greater the number of EADs that have periodic orbits of that family. This fact fits perfectly with what is observed in Fig. 3. The sequence of isolas ends at a value of G_K very close to 0.0331, the value of the left Hopf bifurcation point. It should be noted that, to the left of the isolas represented in the figure, there are more isolas that have not been represented since, as mentioned above, their size is decreasing.

Now we move from left to right. At the left subcritical Hopf bifurcation point ($G_K \approx 0.0331$), the green family of periodic orbits is born unstable and evolves until it disappears at the homoclinic-2 bifurcation point. Orbits in this family experience a single peak (no EADs) and the plateau time grows as the family approaches the homoclinic point. The unstable equilibria curve recovers its stability at right Hopf bifurcation point ($G_K \approx 0.445$). Note that where the blue family loses its stability is the origin of the different isolas formed by the different families of periodic orbits with a different number of EADs. However, the green family of periodic orbits created at the left Hopf bifurcation point is not related to the isolas. It is important to remark that the appearance of homoclinic-1 point after the second loop of the blue family is the cause of the change between the continuous spike-adding of the blue family and the discontinuous spike-adding that occurs in the subsequent isolas (see [27] for details). These are the reasons why we commented at the beginning of this section that homoclinic-1 bifurcation is important for the evolution of the EADs, but homoclinic-2 is not.

From our previous numerical studies we know that the first EAD is created on the first loop ($G_k \approx 0.0486$) of the blue family of periodic orbits of Fig. 4. Therefore, in Fig. 5 we study in detail such a loop. Plots (a)–(d) show the continuation results. On plot (a) we use the AUTO L_2 norm and we clearly observe the loop. On the curve we have marked by encircled numbers several selected values where we show the time series (right columns (1–8)). The second plot (b) gives the period of the orbits along the family loop, showing how there is an increase and later a decrease of the period. The color of the line permits to divide it in three pieces remarking the hysteresis process. In the blue branch, the periodic orbits hardly change, for different values of G_K the period is practically the same and the orbit consists of an AP with one EAD. In the red branch, the period of the orbit remains almost constant at the beginning (right part). But, when G_K reaches the hysteresis zone, the period starts to grow rapidly. In this hysteresis window there is coexistence of periodic orbits with and without EADs. The red branch ends when the coexistence ends, that is, for lower values of G_K only APs with one EAD are observed. The magenta branch is responsible of joining both described branches, closing the loop. Plot (c) gives the Interspike Bifurcation Diagram (IBD), a bifurcation diagram showing the times among the different spikes in the orbits. The longest time (upper red branch) corresponds to the time between two APs without EADs, when one extra spike appears in the AP, the largest time is between the EAD and the next AP. At the beginning of the appearance of the new spike, the phase-2 of the AP is quite long and the peak is located at the end of the plateau, therefore the time between both spikes is quite long. Note in the time series on the right that the new spike is formed simply because the plateau has a positive slope and

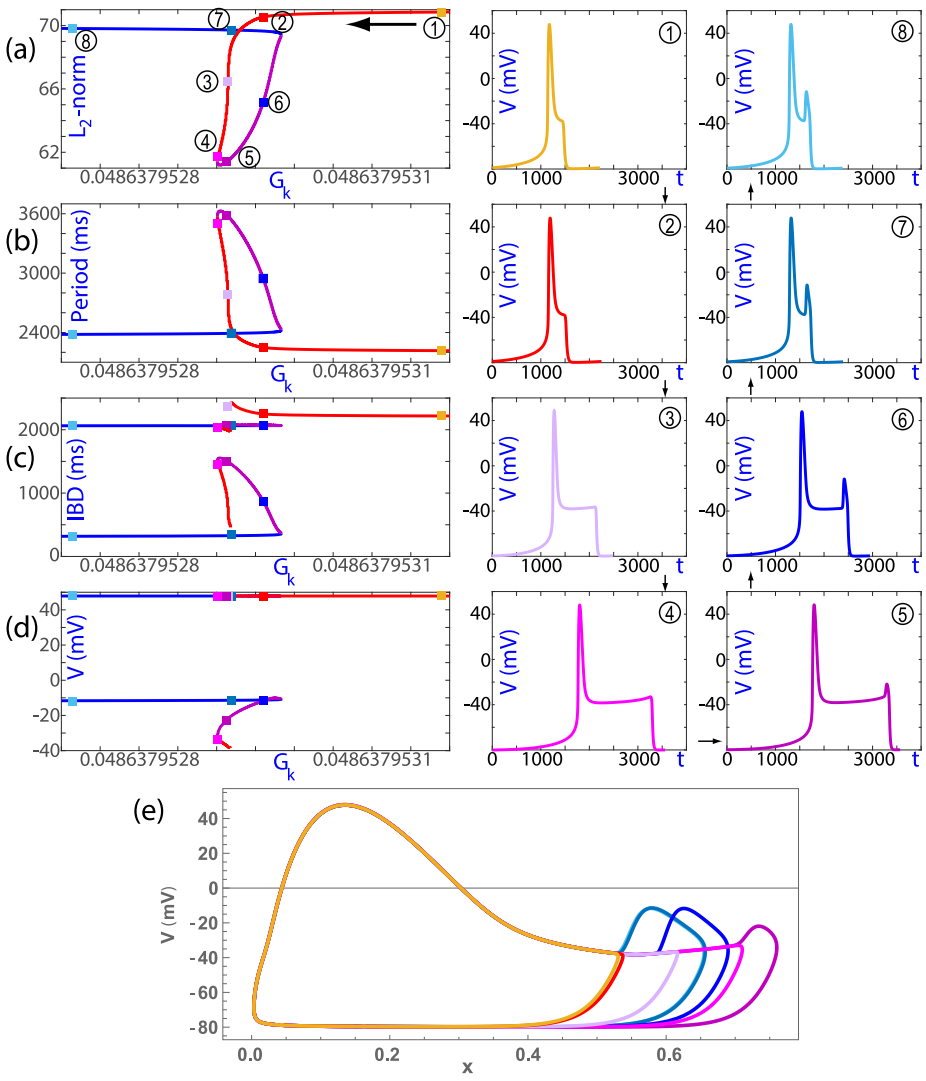

Fig. 5. (a–d) Zoom of the bifurcation diagram from Fig. 4 corresponding to right turn, in the transition on the blue family from no EADs to one EAD. Plots in left column represent the same bifurcation diagram but with different ordinate axis (L_2 norm, period, IBD and V, respectively). Encircled numbers and colored squares mark selected points where time series (right columns (1–8)) and all orbits together (e) have been plotted projected on the plane (x, V). All the figures illustrate the evolution of the periodic orbits throughout the continuous process of generation of the first EAD.

when it ends (and therefore decreases) a maximum is generated (see time series 4). However, we can observe that the situation in time series 5 is very different. In this case, there is a sharp rise and then fall, showing a very marked spike. There we have an EAD. If we look at the location in the diagrams on the left of the selected orbits 4 and 5, we can see how the point at which this EAD is generated is the turning point where the red and magenta branches meet. As the purple branch approaches the blue one, the plateau becomes shorter, approaching the EAD to the main spike of the AP. Plot (d) gives the value of the potential V in each spike for corresponding periodic orbit. Picture (e) presents the projection on the plane (x, V) for all the orbits (1–8) represented on the right. This picture clearly shows how the plateau is elongated in the process of creating the new EAD throughout the hysteresis cycle. It is typical in canard orbits, moving towards the end of the slow manifold and later coming back (we will detail this process in the next section). This process is totally connected with the spike-adding process in the literature of neuron models [12,28]. With this figure, we also detail the location of the point of creation of the EAD.

The second loop on the blue family of periodic orbits has the same behavior as the first but going from one to two EAD. Again, the canard orbits are the mechanism to create the extra spike, which will become the second EAD. As mentioned above, after the second loop at $G_K \approx 0.044$, the family becomes unstable (at $G_K \approx 0.04$) and, after reaching a value close to that of the left Hopf bifurcation point, it turns to the right until it ends up in a homoclinic bifurcation. Throughout this process, the orbit evolves, but no more spikes appear in the orbit.

Now we want to show the complete behavior of the orbits along an isola. In Fig. 6 we study in detail the first one, the orange isola. This isola appears when the family of periodic orbits represented by the blue curve (see Fig. 4(b)) becomes unstable ($G_K \approx 0.04$). Note that, after the second loop in the blue curve takes place, the solutions of that family exhibit two EADs. Central plot (a) shows a zoom of the bifurcation diagram from Fig. 4 using the AUTO L_2 norm. Continuous line is for stable periodic orbits, while discontinuous line is for unstable ones. The stable part is on the upper part of the isola. The rest of plots (b–f) show (x, V) projections of some selected orbits along the isola (the numbers and colors identify the corresponding orbit). The pictures (b2–f2) show time series of the same periodic orbits. We observe several phenomena of the changes of the orbits along the isola. The stable orbits are quite similar (orbits 1, 2 and 3), and similar with the previous orbits of the blue family, but with one extra EAD. But moving from orbit 3 to 4 and 5 we see how the size of the quiescence part is decreasing as G_K decreases. Moreover, from orbit 5 to 6 and 7 the size of the orbit decreases significantly (this can be also seen on the L_2 plot of the

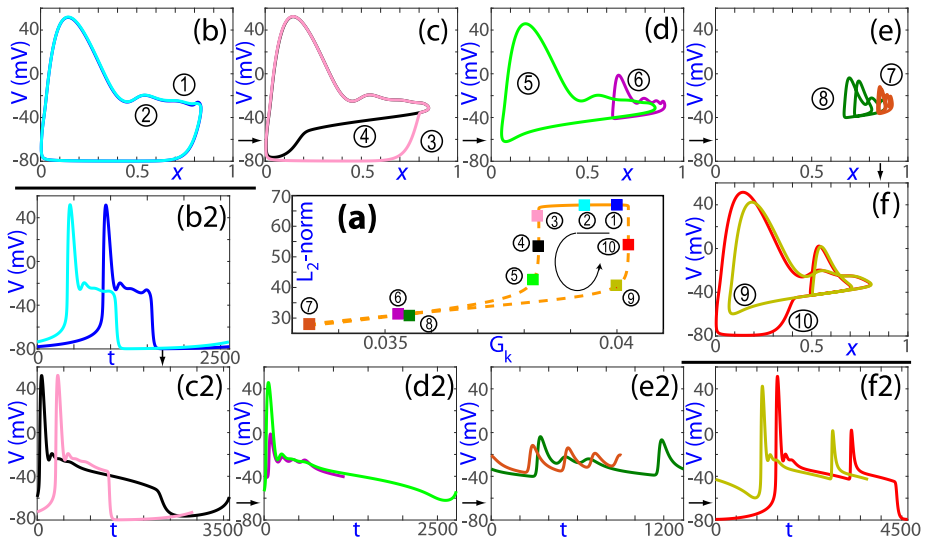

Fig. 6. Center plot (a) shows a zoom of the bifurcation diagram from Fig. 4 corresponding to the first isola, orange isola, with the periodic orbits experiencing three EADs. Encircled numbers and colored squares mark selected points where time series (bottom and left (b2–f2)) and orbits (top and right (b–f)) have been plotted. They show the evolution of the periodic orbits around the isola.

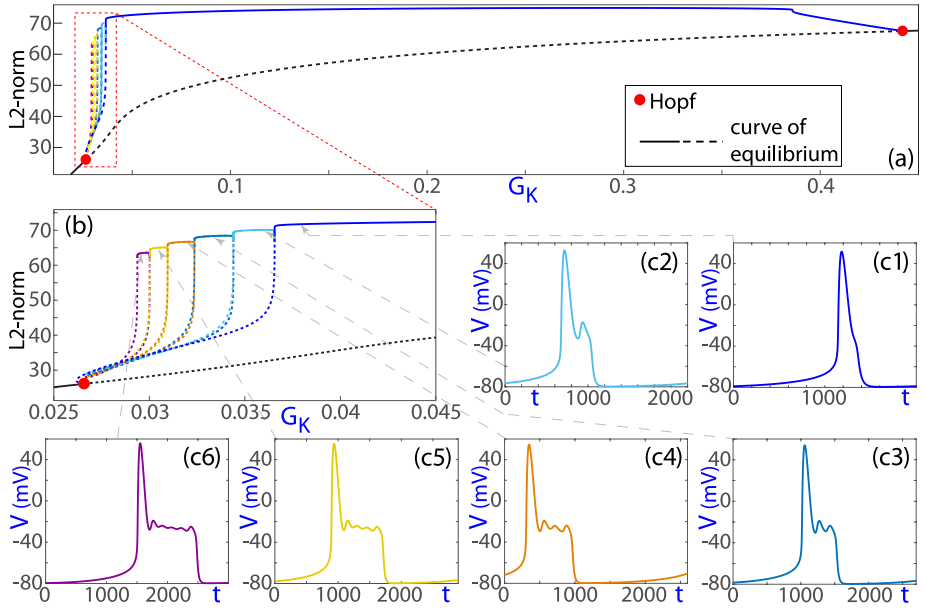

Fig. 7. (a) Bifurcation diagram on the G_K parametric line $E_f = -25$ mV obtained using continuation software AUTO. Black curve represents the equilibrium point. Continuous lines stands for stable invariants, where discontinuous ones unstable. Large blue family of periodic orbits is created and destroyed at two Hopf bifurcation (red) points. The region of periodic orbits with EADs (color families) is located on the left side. (b) Magnification of the region with EADs. (c1–c6) Time series of representative stable periodic orbits for each family.

isola (a)). Finally, the orbits grow again in size (from orbits 8 to 10). We have analyzed the evolution on other isolas and have observed the same process on all of them.

When analyzing Fig. 4, we commented that the presence of homoclinic-1 after the second loop of the blue family caused the spike-adding to stop being continuous and becomes discontinuous, forming isolas. Furthermore, in Fig. 2 we can see that in the lower region of the triangular zone where the different EADs appear there are no homoclinic curves. To analyze what happens in this zone, in Fig. 7(a) we show a bifurcation diagram similar to that in Fig. 4, but along the straight line $E_f = -25$ mV, which does not cut the homoclinic curves. In this case, we can observe how, now, the blue family that is created in the right supercritical Hopf point, ends in the left subcritical Hopf point (see magnification in Fig. 7(b)). Moreover, this family does not undergo any loops. All periodic orbits belonging to such a family are formed by an AP without EADs (c1). When such a family becomes unstable ($G_K \approx 0.0365$), a sequence of isolas starts. The orbits of each isola have a constant number of spikes. Unlike what happened with $E_f = -20$ mV, in this case, the orbits of the first isola have 1 EAD (c2), those of the second 2 (c3) and so on (c4–c6). That is, in this case, all spike-adding is of discontinuous type due to the non-existence of homoclinic bifurcations. This change cannot be detected with the spike-counting technique nor IBD since the number of spikes undergoes the same evolution, an increase as G_K decreases towards the left Hopf point. It is necessary to use continuation techniques in order to detect and explain it.

Thus, we have observed that, when the family of periodic orbits arising from the right Hopf point undergoes a loop, a continuous spike-adding induced by a canard is produced. In contrast, along each isola of periodic orbits, all these orbits have the same number of EADs. The

spike-adding process that occurs in this case between one isola and another is discontinuous and is not induced by a canard. Both types of spike-adding were studied for the Hindmarsh–Rose neuron model in [27]. Moreover, when there are homoclinic curves, their position determines the transition between one type and the other. On the other hand, when there are no homoclinic curves, the spike-adding process is always discontinuous. How orbits evolve during these processes need a much more detailed study, and this will be done with the help of the singular perturbation methods in next section.

3. The role of 2-slow–1-fast and 1-slow–2-fast decompositions

Due to the multi-timescale nature of the model, fast–slow analysis of its dynamics can be performed in different ways. An appropriate formalism for the analysis of systems with different timescales is the geometric singular perturbation theory [29–32], whose main basic idea is the decomposition of dynamics in two differentiated parts: fast and slow. As the system (1) presents three different timescales, two different approaches are possible: either 1 variable is considered fast and 2 variables are slow [7,8], or 2 variables are fast and 1 variable is slow [11]. Both approaches can be combined, which allows for a full 3-timescale description of the model [17–20]. Here we present a brief summary of the application of geometric singular perturbation theory to both situations and combine them to provide a characterization of the observed creation and evolution of EADs.

3.1. Canards and the 2-slow–1-fast decomposition.

Let us first consider a 2-slow–1-fast analysis, with V the fast variable. Geometric singular perturbation theory allows analyzing fast–slow systems via a parameter ϵ that effectively separates, in the limit $\epsilon \to 0$, the fast and slow parts of dynamics. This can be achieved in the reduced Luo–Rudy model (1) identifying $\epsilon = C_m$. The difference in the timescales can be made explicit by introducing a fast time $t' = t/C_m$ in the model and considering the singular limit $C_m \to 0$, which determines the so-called layer system of the problem:

$$\begin{cases} \dfrac{dV}{dt'} = -(I_{Ca} + I_K) = h(V, f, x), \\ \dfrac{df}{dt'} = 0, \\ \dfrac{dx}{dt'} = 0. \end{cases} \tag{2}$$

In these equations, slow variables f and x are fixed and only the fast variable V changes. In consequence, the layer system describes the fast dynamics of the system in the $C_m \to 0$ limit. Fixed points of the layer system conform the critical manifold S_0:

$$S_0 = \left\{(V, f, x) \in \mathbb{R}^3 \mid h(V, f, x) = 0\right\}. \tag{3}$$

Linearization of the layer system on S_0 leads to a system with at least two eigenvalues equal to zero (corresponding to the directions tangent to S_0). On normally hyperbolic regions, the third eigenvalue is either positive or negative, thus defining repelling regions S_0^r and attracting regions S_0^a, respectively. Normal hyperbolicity is lost when all eigenvalues are zero, thus defining the fold manifold

$$L = \{(V, f, x) \in S_0 \mid \partial_V h = 0\}$$

that separates attracting and repelling regions of S_0.

The next step in the analysis is the study of slow dynamics. Consider again the system (1), now without any time-rescaling; the limit $C_m \to 0$ defines the reduced system, which is expressed with respect the original slow time t:

$$\begin{cases} 0 = h(V, f, x), \\ \dfrac{df}{dt} = \dfrac{f_\infty(V) - f}{\tau_f} = g_f(V, f), \\ \dfrac{dx}{dt} = \dfrac{x_\infty(V) - x}{\tau_x} = g_x(V, x). \end{cases} \tag{4}$$

Notice that, unlike (2), the reduced system only presents two differential equations and a constraint to the critical manifold S_0. In other words, the reduced system governs the evolution of slow variables f, x when the fast variable V is already at the equilibrium. Solutions to the reduced systems describe slow dynamics of the system, with a different timescale to that of fast dynamics and where the fast variable V evolves instantaneously to the equilibrium for any change in f and x.

A combination of fast and slow dynamics provides a first approach to the description of orbits of these systems [8]. Far from S_0, only the fast variable V evolves, according to (2); the system is in a fast-dynamic phase and evolves towards S_0^a. When V reaches the equilibrium, slow dynamics starts; slow variables f and x evolve according to (4) and V adapts very quickly towards its equilibrium. If the system does not reach a global equilibrium, eventually the fold manifold L will be reached. Typically, this will result in the system being repelled from the critical manifold S_0 and entering a new phase of fast dynamics, repeating the cycle.

It is possible in some situations to cross from S_0^a into the repelling region S_0^r. The reduced system (4) can be desingularized introducing a new time variable s such that $dt = -\partial_V h\, ds$. The desingularized system introduces a time-inversion on S_0^r, but not on S_0^a, and it is not properly defined on L; as a consequence, equilibria of the desingularized system that are not equilibria of the full system (1), called folded nodes, lay on L and allow for trajectories crossing from S_0^a to S_0^r, called singular canards [33,34]. The system (1) presents a single folded node relevant for the dynamics; see [8] for a detailed characterization.

The 2-slow–1-fast decomposition permits explaining how the small oscillations emerge from the folded node. According to Fenichel's theorem [29], normally hyperbolic regions of the critical manifold are preserved under small perturbations. Therefore, there exist slow attracting S_ϵ^a and repelling S_ϵ^r manifolds obtained as perturbations of the attracting and repelling regions of the critical manifold, respectively. These slow manifolds are the surfaces that contain the slow segments of the periodic orbits of the system for $\epsilon > 0$. Near the fold points of the critical manifold, and due to the loss of normal hyperbolicity, slow manifolds twist around them and cross each other several times [33,35,36]. These intersections are called maximal canards, and they partition the slow manifolds in regions with different number of EADs. The connection between EADs and maximal canards has already been described in several works [37–39], and in particular applied to the description of EADs in the reduced 3-variable Luo–Rudy model [7,8].

To illustrate this, we show in Fig. 8 the relative location of the periodic orbit and the maximal canards on one section of the attracting (green) and repelling (red) slow manifolds. We present on the largest picture (a) on the middle a zoom of the upper part of the bifurcation diagram from Fig. 4. It corresponds to the final stable part of the blue family of periodic orbits and the upper part of the first isolas. Red points mark the parametric values for the rest of pictures. Top and bottom plots show the intersection of the attracting and repelling slow manifolds in green and red color, respectively with a plane transversal to the fold line L (the connecting line among the attracting and repelling sheets, S_0^a and S_0^r of the critical manifold S_0) and passing through the folded node. These curves have been obtained with the continuation software AUTO for selected values of G_K using the computation method detailed in [40]. On these curves we show the intersections of both branches, giving rise to the maximal canards $\gamma_0, \gamma_1, \gamma_2, \ldots$, and the intersection of the periodic orbit Γ. This approach was used in [8,37] for two simplified Luo–Rudy models and also in [41] for a comparison with a high dimensional cardiomyocyte model. From right to left, the first red point is in the region where the periodic orbit does not have any EAD. We show in (b1) how Γ is in the corresponding interval to the left of γ_0. When Γ crosses γ_0, the first EAD appears (b2), and we have a plateau of orbits with just one EAD (see on plot (b3) how Γ is approaching to γ_1, but it does not cross it). Later it cross and periodic orbits have two EADs (b4). Up to now we have a continuous family with

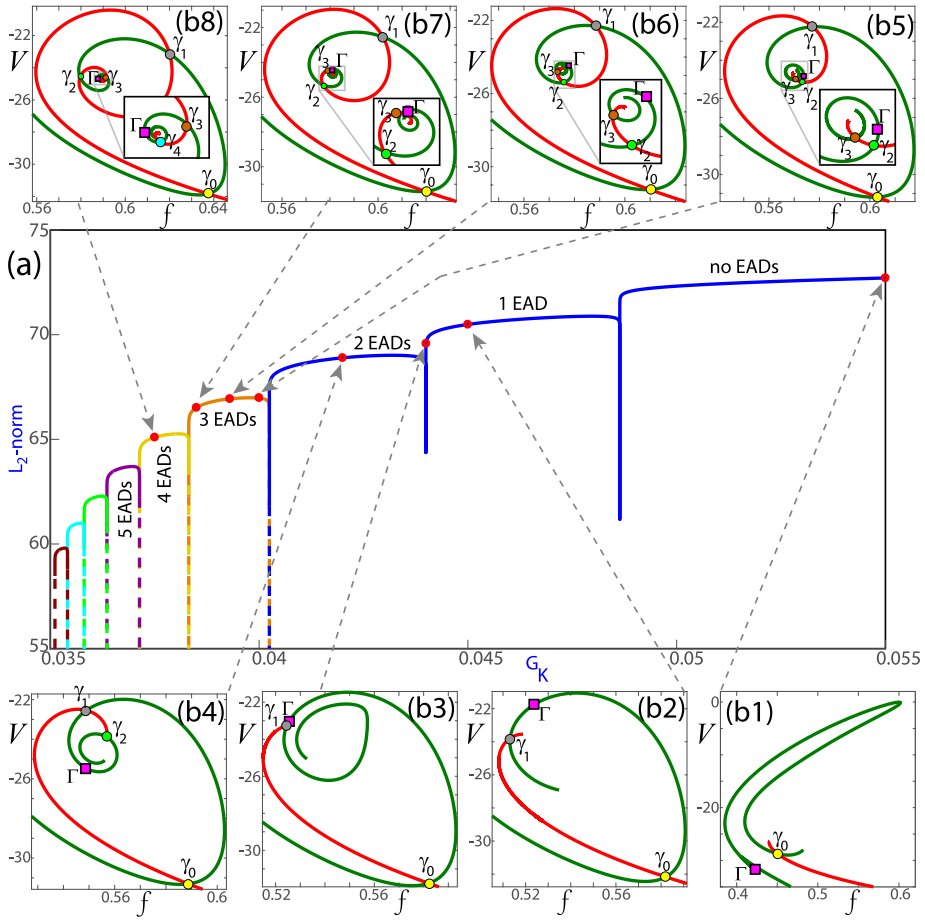

Fig. 8. In the middle plot (a), zoom of the continuation diagram from Fig. 4. Red points mark the parametric values for the rest of pictures. Top and bottom plots show the intersection of the attracting and repelling slow manifolds in green and red color with a plane transversal to the fold line, the intersection of both manifolds (γ_i, the first maximal canards) and the intersection Γ of the periodic orbit.

two loops in the bifurcation lines that are the regions where the first and second EADs are created. Therefore, we observe how the 2-slow–1-fast decomposition explains quite well the location of the creation points of new extra EADs and the admissible number of EADs and gives a good approximation of where it takes place. Besides, on the previous section we have shown in detail how in the loops the extra EADs are created and we can link this precise location with the crossing of Γ and γ_i. Further to the left we enter in the isolas region. On each isola, Γ is in the corresponding interval (γ_i, γ_{i+1}), and so having $i+1$ EADs (plots (b5)-(b8)). In the case of isolas, we have seen in the previous section that the spike-adding is discontinuous. That is, in this case, Γ does not cross continuously through γ_i. Instead, in an isola Γ is in an interval (γ_i, γ_{i+1}) and, when we move to the next isola, Γ is already in the next interval $(\gamma_{i+1}, \gamma_{i+2})$.

3.2. Beyond the 2-slow–1-fast: a new time scale

The information given by the 2-slow–1-fast analysis is essential in order to describe the dynamics of the system [35]. However, a deeper understanding of this dynamics can be achieved by taking into consideration the difference in the timescales of the slow variables x and f. In other words, after determining the critical manifold S_0 and the corresponding reduced system (4), a new fast–slow analysis may help to describe how the system evolves while it stays on the critical manifold S_0.

Let us start by considering a new time $t'' = \frac{1}{\tau_f} t$; this time t'' is fast when compared to t, but slow with respect to t'. Substituting in (4) and taking the singular limit $\tau_f \to 0$, a new layer problem is obtained:

$$\begin{cases} 0 = h(V, f, x), \\ \dfrac{df}{dt''} = g_f(V, f), \\ \dfrac{dx}{dt''} = 0, \end{cases} \Rightarrow \begin{cases} \dfrac{df}{dt''} = g_f(V_0(f, x), f), \\ \dfrac{dx}{dt''} = 0, \end{cases} \tag{5}$$

with $V = V_0(f, x)$ the value of the fast variable on S_0 obtained from solving $h(V, f, x) = 0$. Its corresponding critical manifold, $\bar{S}_0$, is the set of fixed points of the system. By construction, $\bar{S}_0 \subset S_0$; notice also that this is the same critical manifold obtained for the standard 1-slow–2-fast analysis [11]:

$$\bar{S}_0 = \left\{ (V, f, x) \in \mathbb{R}^3 \mid h(V, f, x) = 0,\ g_f(V, f) = 0 \right\}. \tag{6}$$

Regions of this super-slow critical manifold $\bar{S}_0$ can be classified in terms of the stability of the system. The non-zero eigenvalue of the Jacobian matrix of system (5) on $\bar{S}_0$ is

$$\lambda_1 = \left(\frac{\partial g_f}{\partial f}(V, f) - \frac{\dfrac{\partial g_f}{\partial V}(V, f) \dfrac{\partial h}{\partial f}(V, f, x)}{\dfrac{\partial h}{\partial V}(V, f, x)} \right) \Bigg|_{\bar{S}_0}. \tag{7}$$

Computing the value of λ_1 shows that $\bar{S}_0$ presents 4 fold points, which divide it in attractive and repelling regions. 2 of the fold points lay on L; one of the fold points is very close to L and the corresponding repelling branch is small (see Fig. 9). The manifold $\bar{S}_0$ shows three attracting branches: two of them, $\bar{S}_0^{a1}$, $\bar{S}_0^{a3}$, lay on the attracting regions

of S_0, while the third one, $\bar{S}_0^{a2}$, is on the repelling region of S_0. The two repelling branches, $\bar{S}_0^{r1}$, $\bar{S}_0^{r2}$, lay on the repelling region of S_0.

Finally, a reduced system on the super-slow manifold $\bar{S}_0$ is obtained by taking the limit $\tau_f \to 0$ in (4):

$$\begin{cases} 0 = h(V, f, x), \\ 0 = g_f(V, f), \\ \dfrac{d\,x}{d\,t} = g_x(V, x), \end{cases} \tag{8}$$

with t now understood as the super-slow time variable of the system. This reduced system describes the super-slow dynamics on $\bar{S}_0$, with both V and f evolving rapidly towards the equilibrium under changes in x.

From all the above analysis, it is clear that singular dynamics of the three-timescale problem can be roughly divided in three phases, characterized by their speed. Far from S_0, the system has a fast evolution towards attracting regions S_0^a, governed by the layer system (2). Upon reaching it, the system will remain on S_0 for some time, while evolving with a slow dynamics towards $\bar{S}_0$. Lastly, the system will suffer an ultra-slow evolution along $\bar{S}_0$ governed by (8) until the system, now in a 2-fast–1-slow perspective, can be repelled from S_0. The system then enters a new phase of fast dynamics, or could present canard-like behavior in some situations that remain to be analyzed. Note that a similar analysis has been done previously for neuron models in [17–20].

3.3. Analysis of the emergence of EAD

As an application of the above fast–slow analysis, Fig. 9 shows the critical manifolds S_0 and $\bar{S}_0$ for the parameters indicated in Table 1 and for $G_K = 0.048637953$. That is, we are in the first loop of the blue family of periodic orbits. Here, the family changes from an AP without EADs to an AP with an EAD. The 2-dimensional critical manifold S_0 has (for $x > 0$) two stable regions and one unstable region (striped in the figures), separated by two red dashed lines which form the fold manifold L. The one-dimensional critical manifold $\bar{S}_0$ is shown in black; its attracting sets are shown as continuous black curves, and its repelling one as a discontinuous black curve.

Over this geometrical objects, several periodic orbits for G_K between 0.0486379528 and 0.0486379531 are shown. These periodic orbits are some of those depicted in Fig. 5, the circled numbers in the bottom panels of Fig. 9 are identified by the numbering in Fig. 5. A detailed analysis of these trajectories shows how both the 2-slow–1-fast and 1-slow–2-fast analyses complement each other to completely characterize the dynamics of the different orbits.

Starting on the stable region of S_0 for low voltage V, we can see the effect of the three different timescales of the problem: fast dynamics associated to V ensure that the system remains on this branch until it reaches the fold manifold L; additionally, while on S_0, the system evolves towards the slow critical manifold $\bar{S}_0$, as expected; and, when on $\bar{S}_0$, it very slowly moves along it in all cases until the fold manifold is reached. Let us look at this in detail in the selected orbits. We start in the low-voltage stable branch of $\bar{S}_0$, when the orbit reaches the fold manifold L, it is ejected from S_0 with V growing rapidly. Both x and f are approximately constant until the system is again close to the critical manifold S_0. Ideally, once the system lays on S_0, the system should behave as a 2-variable fast–slow system on a surface and approach the attracting branch $\bar{S}_0^{a1}$ of $\bar{S}_0$. This is not, however, what is observed, mainly due to C_m being too large for the approximation to be valid in this range of values. Indeed, figures in the middle row of Fig. 9 show that for high voltages the orbits are far from S_0. Nevertheless, it is noticeable that $\bar{S}_0$, as part of the nullcline of f, separates regions with increasing and decreasing f, which affects the possible behavior of the system. When orbits leave S_0 in a region with negative $\frac{df}{dt}$ (second maximum of orbits 5, 6 and 8 in Fig. 9; see bottom row), the system separates very fast from S_0 and no EAD can occur. Instead, when $\frac{df}{dt}$ is positive (every other case in Fig. 9), loops can occur.

After crossing the fold manifold L, the system is not immediately repelled. Instead, the orbits lay close to the repelling region of S_0, evolving towards the attracting branch $\bar{S}_0^{a2}$. Orbits 1 and 8 are stable and, upon reaching $\bar{S}_0^{a2}$, are immediately ejected into a stable zone of S_0. Orbit 1 being in the zone before γ_0 (see Fig. 8) drops directly into the low-voltage stable zone. In contrast, orbit 8, which is already in the area behind γ_0, undergoes an EAD, i.e. it is attracted to the high-voltage area before descending to the low-voltage stable region of S_0. The remaining orbits are unstable and the trajectory of the system remains close to $\bar{S}_0^{a2}$ for varying times. The changes in the values of G_K determine the behavior of the canard trajectories. In particular, when the trajectory gets ejected from the attracting region of S_0, it can be attracted to either of the two stable regions. That depends on whether the section Γ is before or after γ_0. Orbits 3 and 4 are in the former case, while orbits 5 and 6 are in the latter. No orbit remains on $\bar{S}_0$ once it becomes unstable; the limit case occurs when a trajectory reaches q_2 (between trajectories 4 and 5). The latter reach again the high-voltage stable region and show an EAD. Notice that, in these cases, trajectories evolve again approximately on the top stable critical manifold S_0 until they reach the fold manifold L, and then they are ejected towards the low-voltage stable region of S_0.

It is noticeable that both, the 2-slow–1-fast and 1-slow–2-fast analysis, represented respectively by the critical manifolds S_0 and $\bar{S}_0$, are complementary in order to describe the dynamics. The first spike in each trajectory is determined by the nature of the 2-dimensional manifold S_0 and its fold manifold, as well as part of the trajectory along its unstable region (from the fold manifold to the fixed point [12]). However, the manifold $\bar{S}_0$ determines how the system behaves afterwards.

3.4. Canard evolution along an isola with EADs

Now, in Fig. 10, we focus on the analysis along the first (orange) isola. As in Fig. 9, we show the critical manifolds S_0 and $\bar{S}_0$ and, in this case, some of the periodic orbits from Fig. 6 are drawn on them. Again, we can see how both the 2-slow–1-fast and 1-slow–2-fast analysis are useful in order to describe the characteristics of these trajectories. Let us begin by analyzing the largest trajectory, numbered as 1 and shown in blue in the top row of Fig. 10. In all orbits, time evolution follows the clockwise direction. Starting on the low voltage region, the system is ejected from it when the fold manifold is reached. After a fast increase in voltage, the system gets close to the high-voltage stable region of S_0. While on this region, the system approaches the top stable branch of $\bar{S}_0$, makes several excursions between the stable and the unstable part of S_0, touching in each of them the upper branch of $\bar{S}_0$ (these excursions form the 3 EADs of the orbit) and, finally it is ejected from the unstable region of S_0, when the upper branch of $\bar{S}_0$ becomes unstable, and returns to the low-voltage stable branch of $\bar{S}_0$.

The rest of selected orbits are unstable. Orbits from 2 to 9 enter the repelling region of S_0 remaining for a certain time on $\bar{S}_0^{a2}$ before dropping to the low-voltage region (trajectories 4 and 10) or they are even directly ejected to the high-voltage region without ever descending to the lower stable branch (trajectories 5–9). No trajectory remains on the unstable region of S_0. Notice that the folded node p of the critical manifold S_0 indicates approximately the crossing point for orbits from stable to unstable regions of S_0, which can be interpreted in terms of singular canards. The relevance of singular canards in this analysis will be studied in detail in future works.

Note that all orbits are in the same interval (γ_2, γ_3), so they experience 3 EADs. However, the EADs experienced by the left branch (5 and 6) and right branch (8–10) orbits are different. In the first case, the situation is similar to that described for orbit 1. That is, the orbit makes three excursions between the unstable part of S_0 and the stable branch of $\bar{S}_0$. It is at that point that they separate from orbit 1 since they go

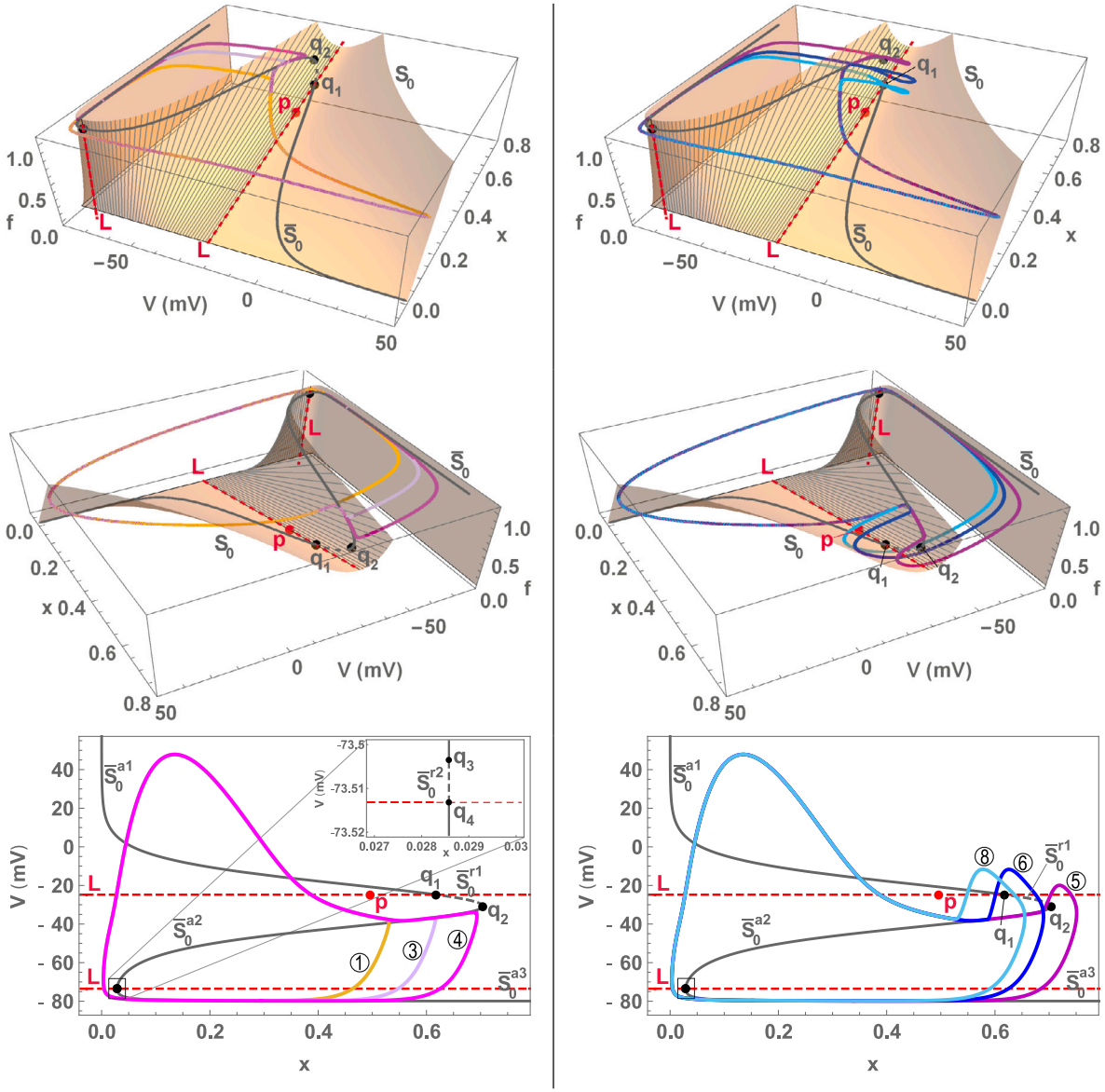

Fig. 9. Trajectories 1, 3, 4 (left column), 5, 6, 8 (right column) from Fig. 5, together with critical and fold manifolds of the model. Top and middle rows show, from different perspectives, the critical manifold S_0 (surface) and $\bar{S}_0$ (black curve), together with the fold manifold L (red dashed lines) and folded node p, for $G_K = 0.048637953$. Unstable regions of S_0 are indicated as stripped surfaces. Super-slow critical manifold $\bar{S}_0$ is unstable between points q_1 and q_2 (branch $\bar{S}_0^{r1}$), and between q_3 and q_4 (branch $\bar{S}_0^{r2}$); these two fold points are very close to each other, as shown in the global figure and in the magnification. Bottom row shows the projections of the trajectories and the $\bar{S}_0$ manifold onto the $x - V$ plane.

down to the unstable region of S_0 before reaching the starting point of the orbit. In contrast, we can see how orbits 8, 9 and 10 experience their third EAD in a second loop. That is, the behavior starts similarly to the one described above, but they only experience 2 EADs before starting to return along $\bar{S}_0^{a2}$. After a time of descent along this branch, the orbit is launched to the upper stable region of S_0, where it descends again towards $\bar{S}_0^{a2}$. This time the descent along this branch connects, finally, with the starting point of the periodic orbit, restarting the cycle. We observe how, small variations in $\bar{S}_0^{a2}$ can produce large changes in the shape of the orbit because the outflow of the unstable region of S_0 can be to either of the two stable regions of S_0. Although an evolution in the orbits along the isola is clearly observed, all of them show canard properties that are only understood by making use of the critical manifold $\bar{S}_0$ derived from the 1-slow–2-fast analysis and all of them experience the same number of EADs because they are in the same region determined by the 2-slow–1-fast decomposition.

Conclusions

In this work, we conducted a detailed investigation into the dynamics of cardiac early afterdepolarizations (EADs) using the reduced Luo–Rudy cardiomyocyte model. By employing the spike-counting sweeping technique, we identified the region of interest in the parametric space where beats with or without EADs occur. Through continuation techniques, we detected the main bifurcations that influence the appearance of these orbits. Moreover, we confirmed that the location of specific homoclinic bifurcations plays a crucial role in determining the type of spike-adding observed in the generation of EADs [27]. Specifically, we observed that on one side of the homoclinic-1 bifurcation, the generation of EADs is continuous and induced by canards, while on the other side, the process is discontinuous, resulting in isolas of periodic orbits with a constant number of EADs.

Considering the distinct timescales of the three variables in the model, we use two possible fast–slow decompositions: the 1-slow–2-fast decomposition and the 2-slow–1-fast decomposition. Our findings

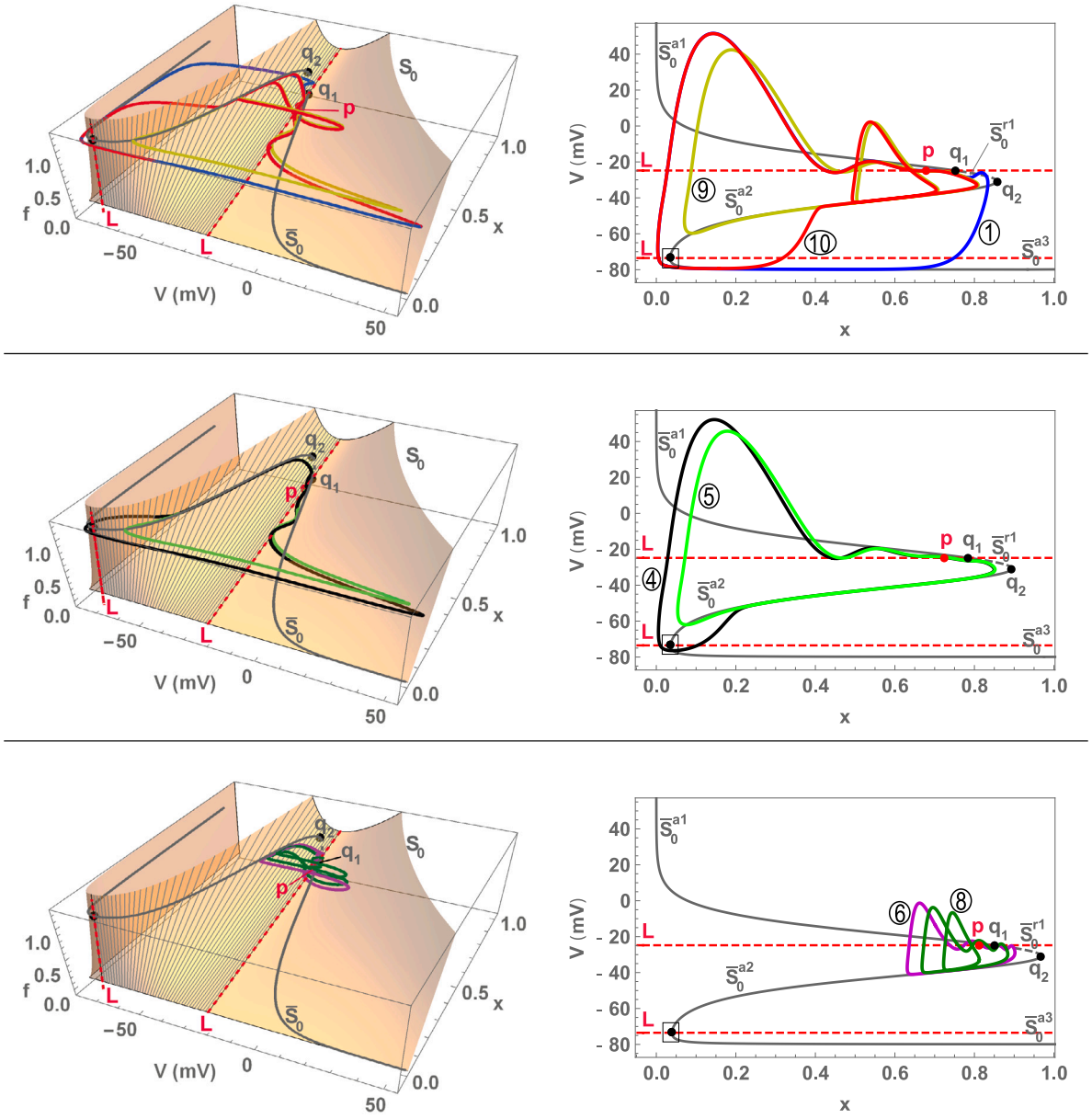

Fig. 10. Sets of trajectories from Fig. 6, together with critical and fold manifolds of the model, illustrating their effect on the dynamics of the system along an isola. In each set, a fixed value of G_K is taken to compute the manifolds: $G_K = 0.04$ for the top row; $G_K = 0.00383$ for the middle row; $G_K = 0.0354$ for the bottom row. The trajectories included in each row occur for values of G_K close to the indicated values (see Fig. 6). Left column shows the critical manifold S_0 (surface) and $\bar{S}_0$ (black curve), together with the fold manifold L (red dashed lines) and folded node p. Unstable regions of S_0 are indicated as stripped surfaces and dashed curves, respectively. Super-slow critical manifold $\bar{S}_0$ is unstable between points q_1 and q_2 (branch $\bar{S}_0^{r1}$), and between q_3 and q_4 (branch $\bar{S}_0^{r2}$, not shown); these two fold points, encased in the black square, are very close to each other, and can be seen in the left-bottom graph of Fig. 9. Right column row shows the projections of the trajectories and the $\bar{S}_0$ manifold onto the $x - V$ plane.

revealed, contrary to what one might think, that these decompositions are not mutually exclusive but rather complementary in explaining the emergence and evolution of EADs across the parametric plane.

Declaration of competing interest

The authors declare that they have no known competing financial interests or personal relationships that could have appeared to influence the work reported in this paper.

Acknowledgments

RB, JJ, MAM and SS have been supported by the Spanish Research project PID2021-122961NB-I00. RB, MAM and SS have been supported by the Spanish Research project TED2021-130459B-I00 and by the European Regional Development Fund and Diputación General de Aragón (E24-20R and LMP94-21). SS has been supported by the Spanish Research project PID2019-105674RB-I00. LP has been supported by the Spanish Research project PID2020-113052GB-I00.

References

[1] Z. Zhang, Z. Qu, Mechanisms of phase-3 early afterdepolarizations and triggered activities in ventricular myocyte models, Physiol. Rep. 9 (11) (2021) e14883.

[2] C.H. Luo, Y. Rudy, A model of the ventricular cardiac action potential, Depolarization, repolarization, and their interaction, Circ. Res. 68 (6) (1991) 1501–1526.

[3] C.H. Luo, Y. Rudy, A dynamic model of the cardiac ventricular action potential. II. Afterdepolarizations, triggered activity, and potentiation, Circ. Res. 74 (6) (1994) 1097–1113.

[4] D. Sato, L.H. Xie, A.A. Sovari, D.X. Tran, N. Morita, F. Xie, H. Karagueuzian, A. Garfinkel, J.N. Weiss, Z. Qu, Synchronization of chaotic early afterdepolarizations in the genesis of cardiac arrhythmias, Proc. Natl. Acad. Sci. 106 (9) (2009) 2983–2988.

[5] R. Barrio, M.A. Martínez, S. Serrano, E. Pueyo, Dynamical mechanism for generation of arrhythmogenic early afterdepolarizations in cardiac myocytes: Insights from in silico electrophysiological models, Phys. Rev. E 106 (2) (2022) 024402.

[6] D.X. Tran, D. Sato, A. Yochelis, J.N. Weiss, A. Garfinkel, Z. Qu, Bifurcation and chaos in a model of cardiac early afterdepolarizations, Phys. Rev. Lett. 102 (2009) 258103.

[7] P. Kügler, A.H. Erhardt, M.A.K. Bulelzai, Early afterdepolarizations in cardiac action potentials as mixed mode oscillations due to a folded node singularity, PLoS ONE 13 (12) (2018) e0209498.

[8] T. Vo, R. Bertram, Why pacing frequency affects the production of early afterdepolarizations in cardiomyocytes: An explanation revealed by slow-fast analysis of a minimal model, Phys. Rev. E 99 (2019) 052205.

[9] T.Y.H. Kitajima, Bifurcation analysis on a generation of early afterdepolarization in a mathematical cardiac model, Int. J. Bifurcation Chaos 31 (12) (2021) 2150179.

[10] Y. Kurata, K. Tsumoto, K. Hayashi, I. Hisatome, Y. Kuda, M. Tanida, Multiple dynamical mechanisms of phase-2 early afterdepolarizations in a human ventricular myocyte model: Involvement of spontaneous sr ca2+release, Front. Physiol. 10 (2020).

[11] D. Sato, L.-H. Xie, T.P. Nguyen, J.N. Weiss, Z. Qu, Irregularly appearing early afterdepolarizations in cardiac myocytes: Random fluctuations or dynamical chaos? Biophys. J. 99 (3) (2010) 765–773.

[12] R. Barrio, M.A. Martínez, L. Pérez, E. Pueyo, Bifurcations and slow-fast analysis in a cardiac cell model for investigation of early afterdepolarizations, Mathematics 8 (6) (2020) 880.

[13] P. Kügler, M. Bulelzai, A.H. Erhardt, Period doubling cascades of limit cycles in cardiac action potential models as precursors to chaotic early afterdepolarizations, BMC Syst. Biol. 11 (1) (2017) 42.

[14] J. Rinzel, A formal classification of bursting mechanisms in excitable systems, in: E. Teramoto, M. Yumaguti (Eds.), Mathematical Topics in Population Biology, in: Morphogenesis and Neurosciences, Springer, Berlin, Heidelberg, 1987, pp. 267–281.

[15] G.B. Ermentrout, D.H. Terman, Mathematical Foundations of Neuroscience, Springer, New York, 2010.

[16] R. Barrio, M.A. Martínez, S. Serrano, A. Shilnikov, Macro- and micro-chaotic structures in the Hindmarsh–Rose model of bursting neurons, Chaos 24 (2) (2014) 023128.

[17] W. Teka, J. Tabak, R. Bertram, The relationship between two fast/slow analysis techniques for bursting oscillations, Chaos 22 (4) (2012) 043117.

[18] T. Vo, R. Bertram, M. Wechselberger, Multiple geometric viewpoints of mixed mode dynamics associated with pseudo-plateau bursting, SIAM J. Appl. Dyn. Syst. 12 (2) (2013) 789–830.

[19] P. Nan, Y. Wang, V. Kirk, J.E. Rubin, Understanding and distinguishing three-time-scale oscillations: Case study in a coupled Morris-Lecar system, SIAM J. Appl. Dyn. Syst. 14 (2015) 1518–1557.

[20] M. Desroches, V. Kirk, Spike-adding in a canonical three-time-scale model: Superslow explosion and folded-saddle canards, SIAM J. Appl. Dyn. Syst. 17 (3) (2018) 1989–2017.

[21] H. Baldemir, D. Avitabile, K. Tsaneva-Atanasova, Pseudo-plateau bursting and mixed-mode oscillations in a model of developing inner hair cells, Commun. Nonlinear Sci. Numer. Simul. 80 (2020) 104979.

[22] M.C. Sanguinetti, D.S. Krafte, R.S. Kass, Voltage-dependent modulation of ca channel current in heart cells by bay k8644, J. General Physiol. 88 (3) (1986) 369–392.

[23] C. Bladen, S. Mirlohi, M. Santiago, K.M. Longworth, M.S. Banister, M. Connor, Modulation of human t-type calcium channels by synthetic cannabinoid receptor agonists in vitro, Neuropharmacology 187 (2021) 108478.

[24] K. Wei, Z. Loh, M. Liang, T. Soong, Z. Hu, Regulation of cardiovascular calcium channel activity by post-translational modifications or interacting proteins, Pflügers Archiv - Eur. J. Physiol. 472 (5) (2020) 653–667.

[25] E.J. Doedel, R. Paffenroth, A.R. Champneys, T.F. Fairgrieve, Y.A. Kuznetsov, B.E. Oldeman, B. Sandstede, X.J. Wang, Auto2000, http://cmvl.cs.concordia.ca/auto.

[26] E. Doedel, AUTO: a program for the automatic bifurcation analysis of autonomous systems, in: Proceedings of the Tenth Manitoba Conference on Numerical Mathematics and Computing, Vol. I (Winnipeg, Man 1980), 30, 1981, pp. 265–284.

[27] R. Barrio, S.F. Ibáñez, L. Pérez, S. Serrano, Classification of fold/hom and fold/hopf spike-adding phenomena, Chaos 31 (4) (2021) 043120.

[28] M. Desroches, T.J. Kaper, M. Krupa, Mixed-mode bursting oscillations: Dynamics created by a slow passage through spike-adding canard explosion in a square-wave burster, Chaos 23 (4) (2013) 046106.

[29] N. Fenichel, Geometric singular perturbation theory for ordinary differential equations, J. Differential Equations 31 (1) (1979) 53–98.

[30] T.J. Kaper, An introduction to geometric methods and dynamical systems theory for singular perturbation problems, Proc. Symp. Appl. Math. 56 (1999) 85–131.

[31] C. Kuehn, Multiple Time Scale Dynamics, Springer, Cham, 2015.

[32] M. Wechselberger, Geometric Singular Perturbation Theory beyond the Standard Form, Springer, Cham, 2020.

[33] M. Wechselberger, Existence and bifurcation of canards in $\mathbb{R}^3$ in the case of a folded node, SIAM J. Appl. Dyn. Syst. 4 (1) (2005) 101–139.

[34] P. De Maesschalck, F. Dumortier, R. Roussarie, Canard Cycles - from Birth to Transition, Springer International Publishing, 2021.

[35] M. Desroches, J. Guckenheimer, B. Krauskopf, C. Kuehn, H.M. Osinga, M. Wechselberger, Mixed-mode oscillations with multiple time scales, SIAM Rev. 54 (2) (2012) 211–288.

[36] P. Szmolyan, M. Wechselberger, Canards in $\mathbb{R}^3$, J. Differential Equations 177 (2) (2001) 419–453.

[37] J. Kimrey, T. Vo, R. Bertram, Big ducks in the heart: Canard analysis can explain large early afterdepolarizations in cardiomyocytes, SIAM J. Appl. Dyn. Syst. 19 (3) (2020) 1701–1735.

[38] J. Kimrey, T. Vo, R. Bertram, Canard analysis reveals why a large Ca^{2+} window current promotes early afterdepolarizations in cardiac myocytes, PLoS Comput Biol 16 (11) (2020) e1008341.

[39] J. Kimrey, T. Vo, R. Bertram, Canards underlie both electrical and ca^{2+}-induced early afterdepolarizations in a model for cardiac myocytes, SIAM J. Appl. Dyn. Syst. 21 (2) (2022) 1059–1091.

[40] M. Desroches, B. Krauskopf, H.M. Osinga, Mixed-mode oscillations and slow manifolds in the self-coupled FitzHugh–Nagumo system, Chaos 18 (1) (2008) 015107.

[41] R. Barrio, M.A. Martínez, E. Pueyo, S. Serrano, Dynamical analysis of early afterdepolarization patterns in a biophysically detailed cardiac model, Chaos 31 (7) (2021) 073137.